BAP1 loss defines a new class of renal cell carcinoma

Samuel Peña-Llopis[1–3], Silvia Vega-Rubín-de-Celis[1–3], Arnold Liao[4], Nan Leng[4], Andrea Pavía-Jiménez[1–3], Shanshan Wang[1–3], Toshinari Yamasaki[1–3], Leah Zhrebker[1–3], Sharanya Sivanand[1–3], Patrick Spence[1–3], Lisa Kinch[5], Tina Hambuch[4], Suneer Jain[4], Yair Lotan[6], Vitaly Margulis[6], Arthur I Sagalowsky[6], Pia Banerji Summerour[3,7], Wareef Kabbani[8], S W Wendy Wong[9], Nick Grishin[5], Marc Laurent[4], Xian-Jin Xie[3], Christian D Haudenschild[4], Mark T Ross[9], David R Bentley[9], Payal Kapur[8] & James Brugarolas[1–3]

The molecular pathogenesis of renal cell carcinoma (RCC) is poorly understood. Whole-genome and exome sequencing followed by innovative tumorgraft analyses (to accurately determine mutant allele ratios) identified several putative two-hit tumor suppressor genes, including *BAP1*. The BAP1 protein, a nuclear deubiquitinase, is inactivated in 15% of clear cell RCCs. BAP1 cofractionates with and binds to HCF-1 in tumorgrafts. Mutations disrupting the HCF-1 binding motif impair BAP1-mediated suppression of cell proliferation but not deubiquitination of monoubiquitinated histone 2A lysine 119 (H2AK119ub1). BAP1 loss sensitizes RCC cells *in vitro* to genotoxic stress. Notably, mutations in *BAP1* and *PBRM1* anticorrelate in tumors ($P = 3 \times 10^{-5}$), and combined loss of BAP1 and PBRM1 in a few RCCs was associated with rhabdoid features ($q = 0.0007$). BAP1 and PBRM1 regulate seemingly different gene expression programs, and BAP1 loss was associated with high tumor grade ($q = 0.0005$). Our results establish the foundation for an integrated pathological and molecular genetic classification of RCC, paving the way for subtype-specific treatments exploiting genetic vulnerabilities.

Kidney cancer is estimated to have been diagnosed in over 60,000 individuals in the United States in 2011 (ref. 1). Most kidney tumors are RCC, and 70% are the clear cell type (ccRCC)[2]. Despite recent advances[3], when metastatic, ccRCC remains largely incurable.

ccRCC is characterized by inactivation of the *VHL* gene (encoding the von Hippel-Lindau protein)[4–6]. *VHL*, which is on chromosome 3p25, is a two-hit tumor suppressor gene. One allele is typically inactivated through a point mutation (or indel), and the other is inactivated through a large deletion resulting in loss-of-heterozygosity (LOH)[7,8]. Also on chromosome 3p is *PBRM1* (encoding Polybromo 1), which is frequently mutated in ccRCC[9]. Other genes implicated in ccRCC development include *SETD2* (ref. 10), *KDM5C*[10] and *KDM6A*[11], but the mutation frequency of each is estimated at <5% (refs. 10,11).

ccRCCs are classified into low- and high-grade tumors[12], and nuclear grade is an important prognostic factor[13,14]. High-grade tumors have mammalian target of rapamycin (mTOR) complex 1 (mTORC1) activation[15]. mTORC1 is a critical regulator of cell growth and is negatively regulated by a complex formed by the tuberous sclerosis complex 1 (TSC1) and 2 (TSC2) proteins[16]. *MTOR*[9,10,17] and *TSC1* (ref. 18) are both mutated in sporadic ccRCC; however, mutations are infrequent[19], and the genetic determinants of tumor grade remain largely unknown.

RESULTS

Identification of candidate two-hit tumor suppressor genes

We sequenced the genome of a sporadic, high-grade ccRCC and paired normal sample to >94% coverage and a mean depth of ≥35× (**Supplementary Figs. 1** and **2**). We found 6,571 somatically acquired single-nucleotide mutations or indels, including 59 in protein-coding regions (**Supplementary Table 1**). Every mutation evaluated was confirmed by Sanger sequencing (**Table 1** and **Supplementary Table 2**). However, mutant allele ratios (MARs)—the fraction of mutant over mutant and wild-type alleles for each mutation—were low; few mutations reached a MAR of 0.5 (expected for heterozygous mutations), and no mutations reached 1 (expected for mutations accompanied by LOH) (**Table 1** and **Supplementary Table 2**). For *VHL*, the MAR was 0.52 (**Fig. 1a** and **Table 1**), which suggested a heterozygous mutation. However, these results conflicted with DNA copy-number analyses showing that one copy of 3p was lost (**Fig. 1b**). We attributed the low MARs to tumor contamination by normal stroma. Contamination occurred despite careful sample selection (**Supplementary Fig. 2c**).

Tumor implantation in mice expands the neoplastic compartment, whereas human stroma is replaced by the host[20]. Therefore, tumorgrafts may be used to calculate MARs with accuracy. RCC tumors implanted orthotopically in mice preserve the characteristics of

Table 1 Integrated analysis of a subset of somatic mutations and DNA copy-number alterations in the index subject

Gene	Chr.	Position[a]	Nucleotide change	MARs			Tumor			Tumorgraft			Change
					Sanger sequencing			ASCN			ASCN		
				Illumina	T	TG	PCN	Min	Max	PCN	Min	Max	
C1orf167	1	11767238	G>T	0.38	0.36	1.00	**1.39**	**0.43**	1.00	**1.02**	**0.003**	1.04	Splice site
STK40	1	36593565	C>A	0.30	0.32	1.00	**1.39**	**0.43**	1.00	**1.00**	**0.003**	1.04	p.Met133Ile
VHL	3	10166479	C>G	0.37	0.52	1.00	**1.39**	**0.43**	1.07	**0.98**	**0.003**	1.05	p.Leu158Val
DIAPH1	5	140885872	C>T	0.26	0.20	0.31	**2.53**	0.97	**1.55**	**3.05**	0.97	**2.00**	p.Arg1164Gln
GFPT2	5	179662025	G>A	0.43	0.38	0.65	**2.51**	0.97	**1.54**	**3.05**	0.97	**2.00**	Splice site
CRISPLD1	8	76088864	G>A	0.57	0.56	1.00	2.02	**0.41**	**1.63**	1.98	**0.003**	**2.00**	p.Val200Ile
ADAMTSL1	9	18767566	del9	0.25	0.34	1.00	**1.42**	**0.44**	1.12	**1.01**	**0.004**	1.06	p.Glu1114_Gln1116del
CTNND1	11	57333402	delG	0.36	0.38	1.00	1.74	**0.41**	1.16	1.95	**0.003**	**1.96**	p.Val769Serfs*5
TMEM151A	11	65818643	G>T	0.36	0.18	1.00	1.62	**0.41**	1.16	1.93	**0.003**	**1.96**	p.Cys117Phe
TREH	11	118035289	C>A	0.54	0.50	1.00	1.62	**0.41**	1.19	1.89	**0.003**	**1.96**	p.Gly478Cys
UBE3B	12	108456960	A>T	0.37	0.40	1.00	**1.39**	**0.43**	1.01	**1.00**	**0.003**	1.06	p.Glu1066Tyr
HS6ST3	13	96283428	A>T	0.38	0.38	1.00	**1.39**	**0.43**	1.06	**0.98**	**0.004**	1.04	p.Tyr464Phe
STK24	13	97907504	C>T	0.28	0.38	1.00	**1.39**	**0.43**	1.06	**0.98**	**0.004**	1.04	p.Arg405Gln
C14orf43	14	73275194	del50	0.32	0.35	1.00	**1.39**	**0.44**	1.07	**0.99**	**0.004**	1.05	p.Gln408Glyfs*65
ZNF434	16	3373160	T>C	0.29	0.30	0.55	1.95	**0.41**	**1.57**	1.98	**0.003**	**1.99**	p.Gln384Arg

Mutation analyses of whole-genome sequences from a tumor-normal pair and the corresponding tumorgraft in the index subject. DNA copy numbers were inferred from segmented data at mutation sites. For heterozygous SNPs, min and max represent the ASCNs of the minor and major alleles, respectively. Bold copy numbers denote deletion (PCN < 1.5 or ASCN < 0.5) or amplification (PCN > 2.5 or ASCN > 1.5). Chr., chromosome. A complete list of mutations is provided in **Supplementary Table 2**.
[a]Annotated with NCBI36.1 and Ensembl build 54.

human tumors[21]. We performed Sanger sequencing of mutated genes in a tumorgraft derived from the index subject's tumor using human-specific primers. In comparison to tumor MAR (MAR_T) values, tumorgraft MAR (MAR_{TG}) values often increased to ~0.5, and, for several genes including *VHL*, they reached 1 (**Table 1**, **Supplementary Fig. 3** and **Supplementary Table 2**).

To determine whether MAR_{TG} values reflected those expected in the index subject's tumor, we asked whether a correlation existed between MAR_{TG} and corresponding regional DNA copy numbers in the tumor (**Fig. 1b**, **Table 1** and **Supplementary Table 2**). A correlation was found with MAR_{TG} ($P = 1.3 \times 10^{-5}$) but not with MAR_T ($P = 0.054$). These data suggest that MARs in tumors are more accurately determined by evaluating tumorgrafts. Consistent with the notion that tumorgrafts represent largely pure populations of human tumor cells, paired copy numbers (PCNs) and allele-specific copy numbers (ASCNs) in tumorgrafts more closely approached integer values (**Fig. 1b**, **Table 1** and **Supplementary Table 2**).

To identify putative two-hit tumor suppressor genes, we searched for genes with MAR_{TG} values of ~1. Some genes (*STK40*, *UBE3B*, *HS6ST3*, *STK24*, *C1orf167*, *ADAMTSL1* and *C14orf43*) were in regions of deletion (PCN_TG values of ~1), whereas others (*CRISPLD1*, *TMEM151A*, *TREH* and *CTNND1*) were in areas of copy-neutral LOH (PCN_TG values of ~2; tumorgraft ASCN_min values of ~0 and ASCN_max values of ~2) (**Fig. 1b** and **Table 1**). Because mutations in regions of copy-neutral LOH could be either homozygous (for example, *CRISPLD1*) or heterozygous (for example, *ZNF434*) (**Fig. 1b** and **Table 1**), accurate MARs were essential to establish whether mutated genes were putative two-hit tumor suppressors.

Accurate MARs were also helpful in inferring whether, in areas of duplication (PCN_TG of ~3), the allele amplified was mutated (for example, *GFPT2*; $MAR_{TG} = 0.65$ (expected 0.66)) or wild type (for example, *DIAPH1*; $MAR_{TG} = 0.31$ (expected 0.33)) (**Table 1**). In the case of *GFPT2*, the mutation may have preceded the duplication, whereas in the case of *DIAPH1*, the mutation is likely to have followed the duplication. Thus, analyses in tumorgrafts identified candidate tumor suppressor genes and shed light on the temporal sequence of mutation acquisition.

Evaluation of somatically mutated genes in a discovery cohort
Twenty-one genes mutated in the sequenced ccRCC tumor and not previously examined by the Sanger Institute[10] were sequenced in a discovery set of 76 ccRCCs, and mutations were examined in the corresponding normal samples (**Supplementary Table 3**). As determined by *VHL* sequencing, which revealed somatically acquired mutations in 79% of tumors (**Supplementary Data 1**), sensitivity for mutation detection was excellent. Several putative two-hit tumor suppressor genes were mutated at higher than expected frequencies, including *CRISPLD1*, which was mutated in two additional tumors ($q = 0.044$), and *TMEM151A*, mutated in three additional tumors ($q = 0.005$). In addition, several other genes were recurrently mutated, including *OCA2* and *ND1* (also known as *MT-ND1*) (**Supplementary Table 4**). Germline mutations in *OCA2* cause autosomal recessive oculocutaneous albinism type 2, and the two somatic mutations we identified (encoding p.Pro211Leu and p.Val443Ile alterations; **Supplementary Table 4**) are known disease-causing mutations[22,23]. Two additional somatically acquired mutations were found in mitochondrial *ND1* (**Supplementary Table 4**), a gene mutated in oncocytomas, a benign tumor type[24]. The presence of these mutations in ccRCC suggests that oncocytomas could transform into malignant tumors. Transformation may result from *VHL* inactivation, which was observed in all the tumors with somatic *ND1* mutations (**Supplementary Data 1**). *VHL* inactivation could change the morphological appearance of the tumor by affecting cellular metabolism and angiogenesis. In addition, three mutations were identified in *TSC1*, which we previously reported[18].

Exome sequencing identifies two-hit tumor suppressor gene *BAP1*
We performed exome sequencing of seven ccRCC primary tumors, including six of high grade, and corresponding normal samples. A metastasis from one affected individual was also sequenced. We found 345 somatically acquired mutations (**Supplementary Table 5**). In the tumor-metastasis pair, we observed 37 and 39 mutations, respectively, and 32 were shared.

To determine the accuracy of the mutations called, we performed Sanger sequencing. If concordance was >95%, Sanger sequencing of 82 mutations would predict >90% accuracy for the whole cohort.
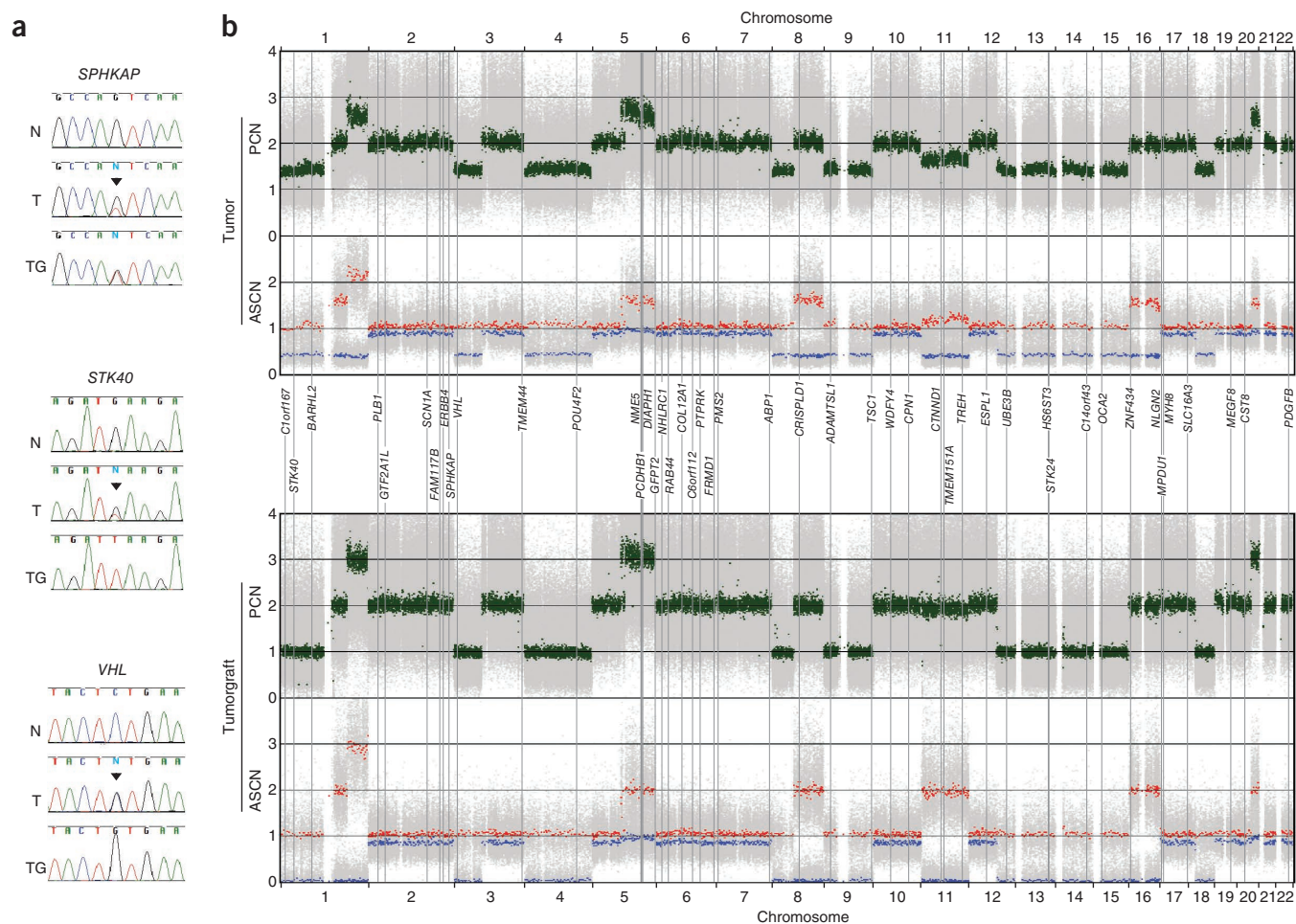
Figure 1 Integrative mutation and DNA copy-number analyses in a tumor and tumorgraft from the index subject. (**a**) Representative capillary sequencing chromatograms of normal (N), tumor (T) and tumorgraft (TG) samples showing different examples of allele enrichment in the tumorgraft. Arrowheads indicate mutations. (**b**) ASCN and PCN representation of high-density SNP array data incorporating the estimated position of mutated genes. Green, paired copy numbers. Red and blue denote maximum and minimum copy numbers, respectively, for each heterozygous SNP.

Among 82 randomly selected mutations, 78 were confirmed with an accuracy of >95% (**Supplementary Table 6** and **Supplementary Data 2**). For 5 tumors, there were tumorgrafts available, and sequencing analyses of mutated genes therein uncovered 16 potential two-hit tumor suppressor genes (**Supplementary Table 6**).

We focused on ten genes mutated in at least two tumors (**Supplementary Table 7**). All mutations were validated by Sanger sequencing. Whereas MAR_T analysis failed to identify any putative two-hit tumor suppressors, another gene in addition to *VHL* and *PBRM1*, *BAP1*, showed MAR_{TG} values of ~1 (**Supplementary Table 7**).

BAP1 sequencing in the discovery set of 76 ccRCCs identified 11 nonsynonymous mutations, including 10 confirmed to be somatically acquired (**Table 2**). Examination of a validation ccRCC set ($n = 92$) with corresponding normal samples uncovered 11 additional non-synonymous mutations, including 10 that were somatically acquired (**Table 2**). Two mutations in tumors without matching normal samples were truncating and likely deleterious. Altogether, the *BAP1* mutation rate was 14% (24/176 tumors). *BAP1* encodes a nuclear deubiquitinase (DUB) of the ubiquitin C-terminal hydrolase (UCH)-domain containing family[25–27] that is mutated in both uveal[28] and cutaneous[29] melanoma, as well as in mesothelioma[30]. In ccRCC, most mutations were predicted to truncate the protein, and mutations were enriched in sequences encoding the UCH domain (**Fig. 2a,b**).

Development of a clinical assay for BAP1 detection

As most mutations were truncating, we developed in a laboratory with Clinical Laboratory Improvement Amendments (CLIA) certification an immunohistochemistry (IHC) test for the presence-absence of BAP1 protein. Genetically characterized ccRCC samples validated by protein blot were used as controls (**Fig. 2c,d**). Scoring was performed by a clinical pathologist who was blinded to the *BAP1* genotype. IHC results were interpretable in 175 out of 176 tumors. Nuclear BAP1 was detected in 150 tumors, and 148 were wild type for *BAP1* (**Supplementary Fig. 4**). The two discordant samples had missense mutations (encoding p.Gly13Val and p.Phe170Leu changes). Twenty-five samples were negative by IHC, and 22 of these had *BAP1* mutations. Analysis of an IHC-negative sample that had wild-type *BAP1* by protein blot failed to reveal detectable BAP1 protein, suggesting that other mechanisms exist to inactivate BAP1. Overall, the positive and negative predictive values of the IHC test were ~100% and 98.6%, respectively.

Structural analyses of *BAP1* missense mutations

To evaluate the effects of *BAP1* missense mutations in a structural context, we generated a BAP1 protein model on the basis of the related family members Uch-L3 and Uch37 (**Fig. 2b**). Because ubiquitin binding orders a significant portion of the protein, the UCH domain

Table 2 List of *BAP1* mutations in ccRCCs and cell lines

ID	Coding sequence mutation	Protein
3575	c.5_6dupAT	p.Lys3Ilefs*33
63	c.21_32del12	p.Glu7Asp,Leu8_Asp11del
T145	c.38G>T	p.Gly13Val[a]
T211	c.58G>T	p.Glu20*
T16	c.128T>G	p.Val43Gly
T114	c.193delT	p.Leu65Trpfs*7
T166	c.283G>C	p.Ala95Pro
T69	c.335T>C	p.Leu112Pro
T115	c.430C>A	p.His144Asn
3397	c.IVS438–1G>A	Splice site
T55	c.458delC	p.Pro153Leufs*34
T212	c.510T>A	p.Phe170Leu[a]
T184	c.889G>T	p.Glu297*
209	c.971delC	p.Pro324Hisfs*11
162	c.1219delG	p.Asp407Metfs*42
T149	c.1256delA	p.Lys419Argfs*11
T26	c.1271_1274delGGAA	p.Lys425Glnfs*4
78	c.1793delC	p.Pro598Glnfs*19
9575	c.1981A>T	p.Lys661*
T163	c.2028_2046del19	p.Cys676Trpfs*18
T70	c.2050C>T	p.Gln684*
T25	c.2051delA	p.Gln684Argfs*16
40	c.2134C>T	p.Gln712*
9145	c.2188T>G	p.*730Glyext*206
769-P	c.97T>G	p.Tyr33Asp[a]
UMRC6	c.430delC	p.His144Metfs*94

[a]Missense mutations not affecting protein levels.

of BAP1 was modeled after that of Uch-L3 bound to ubiquitin (Protein Data Bank (PDB) 1xd3). The interaction with the ULD domain was built by superimposing that of Uch37 (PDB 3ihr). Four alterations abrogated protein expression: three were predicted to destabilize the protein (p.Val43Gly and p.Leu112Pro removed side chains that contribute to the hydrophobic core, and p.Ala95Pro disrupted the backbone of a central α helix), and the fourth (p.His144Asn) disrupted the position of a flexible loop (**Fig. 2b**). Two alterations did not abrogate protein expression (p.Gly13Val and p.Phe170Leu). These amino-acid changes disrupted side chains implicated in either an intramolecular interaction with the ULD domain (Gly13) or ubiquitin binding (Phe170) and highlight the importance of these interactions for tumor suppressor function.

BAP1 suppresses RCC cell proliferation

Studies of the role of BAP1 in cell proliferation have given conflicting results[25–27,30–33]. To examine BAP1 in an appropriate context, ccRCC cell lines were sought in which natural selection had led to *BAP1* inactivation. Among 12 RCC cell lines initially examined, only 769-P had a *BAP1* mutation (**Supplementary Table 8**). The mutation (c.97T>G; p.Tyr33Asp) disrupted a residue binding ubiquitin and did not abrogate protein expression (**Figs. 2b** and **3a**).

To determine the role of BAP1, 769-P cells were reconstituted with epitope-tagged wild-type BAP1 (or an empty vector control). BAP1 repressed cell proliferation without causing apoptosis (**Fig. 3a** and data not shown). However, BAP1 did not completely abrogate cell proliferation. To determine whether endogenous, mutant BAP1 acted in a dominant-negative fashion, we depleted endogenous *BAP1* using small hairpin RNA (shRNA). However, depletion of mutant BAP1 did not increase the effects of ectopically expressed wild-type BAP1, indicating that mutant BAP1 did not function in a dominant-negative fashion (**Fig. 3b**).

BAP1 deubiquitinates H2AK119ub1 in renal cancer cells

The protein encoded by the *BAP1* ortholog in *Drosophila melanogaster*, Calypso, targets monoubiquitinated histone H2A (H2Aub1)[34]. An examination of H2AK119ub1 levels in 769-P cells reconstituted with wild-type BAP1 showed downregulation of basal H2Aub1 levels, indicating that mammalian BAP1 deubiquitinates H2A in renal cancer cells (**Fig. 3c**).

HCF-1 binding is required for suppression of cell proliferation

BAP1 interacts with host cell factor–1 (HCF-1)[31,33,35], which serves as a scaffold for several chromatin-remodeling complexes[36]. HCF-1 binds to multiple transcription factors, including several E2Fs[37,38], and recruits histone-modifying enzymes, such as Set1/MLL1 histone methyltransferases[39–41], LSD1 histone demethylase[42], Sin3 histone deacetylase[39] and MOF histone acetyltransferase[43].

We asked whether BAP1 interacted with HCF-1 in 769-P cells. An interaction was confirmed by reciprocal immunoprecipitation experiments (**Fig. 3d**). Notably, HCF-1 immunoprecipitation depleted BAP1 from cell extracts to the same extent as BAP1 immunoprecipitation, suggesting that, as in other cell types[35], the majority of BAP1 in renal cancer cells is bound to HCF-1 (**Fig. 3d**). BAP1 has been proposed to deubiquitinate HCF-1 (refs. 31,33) and regulate HCF-1 levels[31], but, consistent with other reports[33], HCF-1 levels were similar in BAP1-deficient and -reconstituted 769-P cells (**Fig. 3d**).

We mutated sequences in *BAP1* encoding the HCF-1 binding motif and evaluated this mutant (HBM) in cell proliferation assays. HBM suppressed HCF-1 binding and compromised the inhibitory effect of BAP1 on cell proliferation (**Fig. 3e**). However, the HBM mutant did not differ from wild-type BAP1 in its ability to deubiquitinate histone H2A (**Fig. 3f**). Thus, BAP1 binds to HCF-1, and binding to HCF-1 but not H2Aub1 deubiquitination is important for the inhibition of cell proliferation.

Next, we performed gel-filtration chromatography to further examine BAP1-containing complexes. Extracts from 769-P cells expressing either an empty vector or wild-type BAP1 were fractionated using a size-exclusion column and subjected to protein blotting. Most BAP1 was found in complexes of >1 MDa and eluted with HCF-1 (**Supplementary Fig. 5**).

BAP1 loss sensitizes RCC cells to radiation and PARP inhibitors

BAP1 is phosphorylated following DNA damage[44,45], and we asked whether BAP1 loss affected the response to γ-irradiation. 769-P cells with or without wild-type BAP1 showed a similar pattern of foci of Rad51 and H2AX phosphorylated at Ser139 (γH2AX) (**Supplementary Fig. 6a**). However, BAP1-deficient cells were more sensitive to ionizing radiation (**Supplementary Fig. 6b**), and fewer colonies formed in clonogenic assays (**Supplementary Fig. 6c**). In addition, BAP1 loss sensitized cells to the PARP inhibitor olaparib (**Supplementary Fig. 6d,e**).

We examined four additional ccRCC cell lines (**Supplementary Table 8**). UMRC6 lacked BAP1 protein and had a frameshift mutation (c.430delC) (**Supplementary Fig. 7a,b**). As in 769-P cells, (i) cell proliferation was inhibited by wild-type BAP1 and substantially less so by an HBM mutant, (ii) the HBM mutant reduced H2Aub1 levels, (iii) BAP1 cofractionated with HCF-1, and (iv) restoration of BAP1 protected UMRC6 cells against genotoxic death (**Supplementary Fig. 7**).

BAP1 binds HCF-1 and elutes with HCF-1 in tumorgrafts

The usefulness of RCC cell lines is limited by the development of mutations and copy-number alterations as tumor cells adapt to
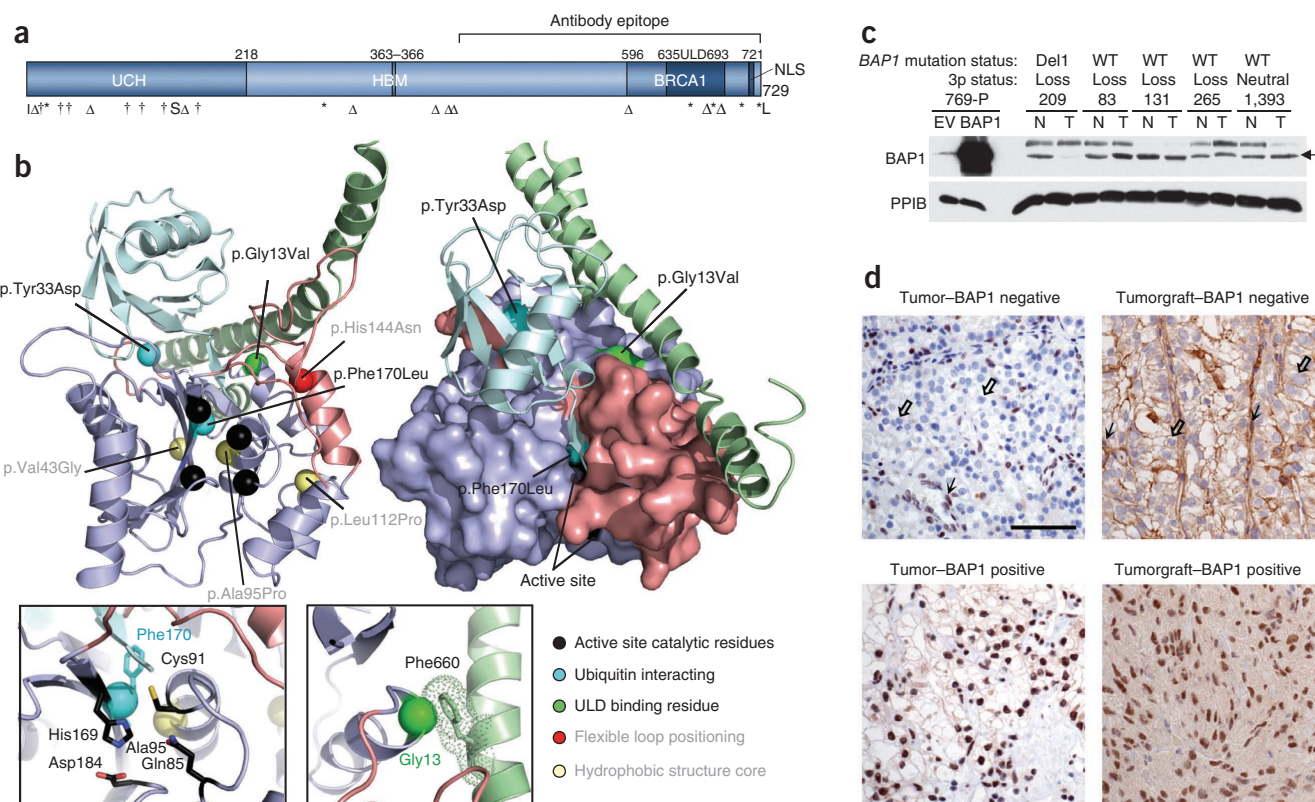
Figure 2 BAP1 is a tumor suppressor in ccRCC. (**a**) Schematic of BAP1 with alterations. BRCA1, putative BRCA1-interacting domain; ULD, Uch37-like domain; NLS, nuclear localization signal; I, insertion; Δ, deletion; †, missense; *, nonsense; S, splice site; *L, stop codon loss. (**b**) Structural model of the BAP1 UCH domain (purple) and ULD tail (green) bound to ubiquitin (cyan); structural elements that alter upon ubiquitin binding are colored salmon. Left, cartoon of BAP1 model: mutated residues abrogating protein expression are labeled in gray. Right, surface representation of BAP1 highlighting the positions of RCC alterations on interaction surfaces. Left inset, enlarged view of the DUB active site. Right inset, enlarged view of the Gly13 interaction with an aromatic residue in the ULD tail (dots indicate interaction radius). (**c**) Protein blots of extracts from tumors with defined *BAP1* mutation and chromosome 3p status. 769-P cells transfected with either an empty vector (EV) or a vector expressing wild-type (WT) BAP1 were used as controls. PPIB (cyclophilin B) is shown as a loading control. Arrow indicates BAP1. (**d**) Representative IHC of tumors and tumorgrafts positive or negative for nuclear BAP1. Scale bar, 50 μm. Open arrows indicate tumor cells; simple arrows indicate endothelial cells and lymphocytes, which express BAP1 and serve as internal controls.

growth in culture[7,46]. Divergence from tumors may be particularly pronounced with respect to epigenetic regulation, as growth conditions of cell lines and tumors are very different. In contrast, the pattern of gene expression in tumors is reproduced in tumorgrafts growing orthotopically in mice[21], and tumorgrafts, like cell lines, represent a renewable source of tumor material. To determine whether the interaction of BAP1 with HCF-1 was physiologically relevant, we analyzed tumorgrafts. As in cell lines, BAP1 was bound to and cofractionated with HCF-1 (**Fig. 4a,b**). In addition, we examined whether there was a correlation between *BAP1* mutation and H2Aub1 levels in tumorgrafts, but no such correlation was observed (**Fig. 4c**). Taken together, these data show that the binding of BAP1 to HCF-1 is likely to be important for BAP1-mediated suppression of RCC development.

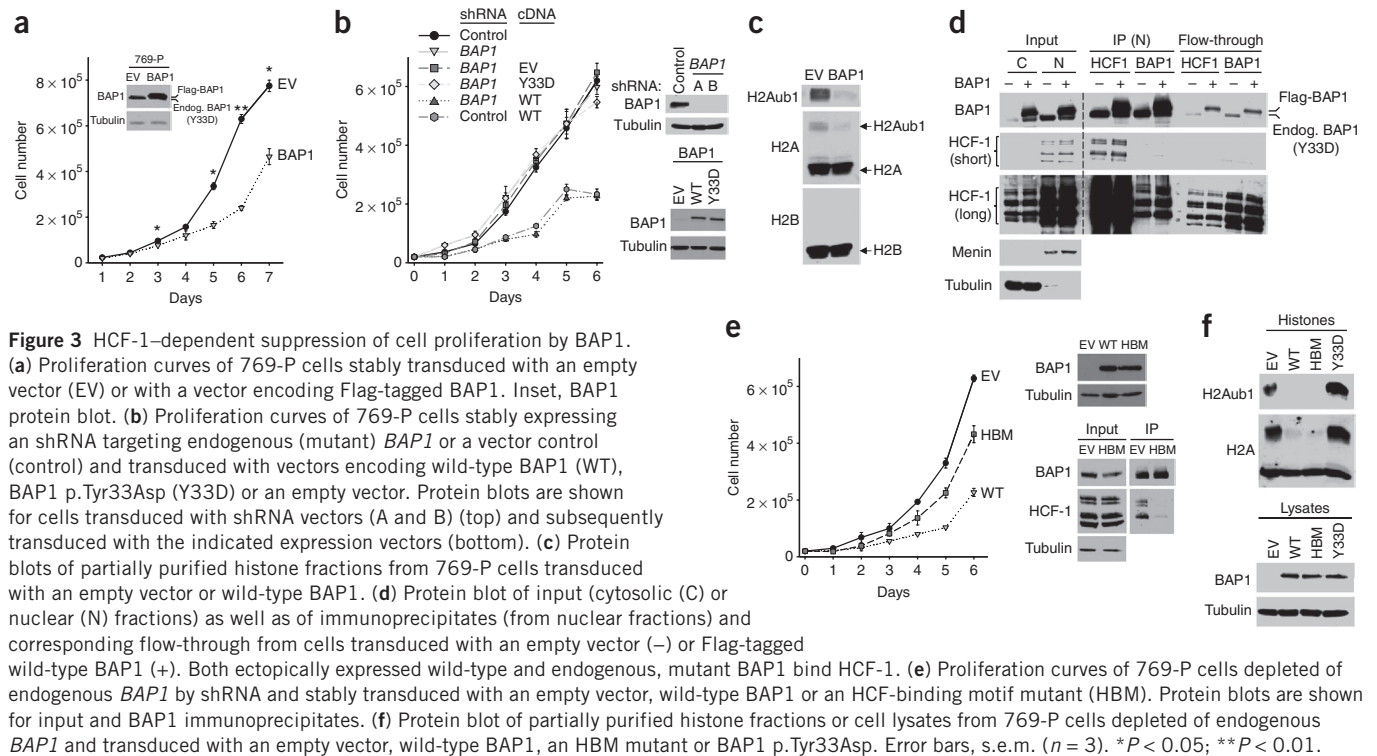## BAP1 loss is associated with high tumor grade

Deep-sequencing studies were largely focused on high-grade tumors. An analysis of all 176 tumors examined showed that BAP1 loss correlated with high Fuhrman nuclear grade ($q = 0.0005$) (**Supplementary Data 1**). Because nuclear grade is associated with mTORC1 activation[15], we tested whether a correlation existed between BAP1 loss and mTORC1 activity. As determined by the phosphorylation of both S6 and 4E-BP1, BAP1 loss was correlated with mTORC1 activation

($q = 3 \times 10^{-4}$ and 0.029, respectively) (**Fig. 5a** and **Supplementary Data 1**). This association did not seem to be direct, however, and similar levels of mTORC1 activation were observed in BAP1-deficient and wild-type BAP1–reconstituted cells (**Supplementary Fig. 8**).

BAP1 and *PBRM1* mutations anticorrelate in ccRCC

To explore whether a relationship existed between loss of BAP1 and PBRM1, we first developed an IHC assay for PBRM1 (also known as BAF180) (**Fig. 5a**). Evaluation of the 176 tumors showed confident PBRM1 staining for 146 samples, and 53% were negative for PBRM1 (**Supplementary Data 1**). As PBRM1 was lost in ~50% of tumors, BAP1 loss should distribute equally between PBRM1-expressing and -deficient tumors. However, only 4 of 21 BAP1-deficient tumors were also deficient for PBRM1 (**Supplementary Fig. 9a**). These results suggest that PBRM1 and BAP1 loss are anticorrelated in tumors ($P = 7 \times 10^{-4}$).

To explore this further, we sequenced *PBRM1* in the 176 ccRCCs. We identified 94 somatic mutations, including 6 missense mutations (**Supplementary Data 1**). Structural analyses of the effects of these mutations are shown in **Supplementary Figure 10**. We correlated sequencing data with the results from IHC: 90% of samples that were negative for PBRM1 by IHC had a mutation, and 90% of the samples that were positive had wild-type sequence ($P = 4 \times 10^{-23}$;

Figure 3 HCF-1–dependent suppression of cell proliferation by BAP1.
(**a**) Proliferation curves of 769-P cells stably transduced with an empty
vector (EV) or with a vector encoding Flag-tagged BAP1. Inset, BAP1
protein blot. (**b**) Proliferation curves of 769-P cells stably expressing
an shRNA targeting endogenous (mutant) *BAP1* or a vector control
(control) and transduced with vectors encoding wild-type BAP1 (WT),
BAP1 p.Tyr33Asp (Y33D) or an empty vector. Protein blots are shown
for cells transduced with shRNA vectors (A and B) (top) and subsequently
transduced with the indicated expression vectors (bottom). (**c**) Protein
blots of partially purified histone fractions from 769-P cells transduced
with an empty vector or wild-type BAP1. (**d**) Protein blot of input (cytosolic (C) or
nuclear (N) fractions) as well as of immunoprecipitates (from nuclear fractions) and
corresponding flow-through from cells transduced with an empty vector (−) or Flag-tagged
wild-type BAP1 (+). Both ectopically expressed wild-type and endogenous, mutant BAP1 bind HCF-1. (**e**) Proliferation curves of 769-P cells depleted of
endogenous *BAP1* by shRNA and stably transduced with an empty vector, wild-type BAP1 or an HCF-binding motif mutant (HBM). Protein blots are shown
for input and BAP1 immunoprecipitates. (**f**) Protein blot of partially purified histone fractions or cell lysates from 769-P cells depleted of endogenous
BAP1 and transduced with an empty vector, wild-type BAP1, an HBM mutant or BAP1 p.Tyr33Asp. Error bars, s.e.m. ($n = 3$). *$P < 0.05$; **$P < 0.01$.

Supplementary Fig. 9b). An analysis of *BAP1* and *PBRM1* muta-
tions in tumors revealed that only 3 of 24 samples with *BAP1* muta-
tions had a somatically acquired *PBRM1* mutation (**Supplementary
Fig. 9c**). Thus, mutations in these two genes were found to anti-
correlate in tumors ($P = 3 \times 10^{-5}$).

For comparison, we evaluated the distribution of mutations in
SETD2 and *KDM5C* with respect to *PBRM1* mutations in ccRCCs
from the Sanger Institute[9,10]. Among 348 ccRCCs genotyped for
PBRM1, 15 mutations in *SETD2* were observed, and these mutations
were distributed equally between tumors with mutant and wild-type
PBRM1 (in 8 and 7 tumors, respectively; **Supplementary Data 3**).
KDM5C mutations were similarly distributed across tumors with
mutant and wild-type *PBRM1* (in five and four tumors, respectively;
Supplementary Data 3).

Combining the IHC and mutation data, 5 out of 27 BAP1-deficient
tumors were found to also be deficient in PBRM1. Assuming a binomial

distribution of BAP1 loss, these data indicate that simultaneous inac-
tivation of BAP1 and PBRM1 is negatively selected for in tumors
($P = 0.0008$). Notably, however, loss of BAP1 or PBRM1 was observed
in 70% of ccRCCs (**Fig. 5b**).

To obtain further insight into the relationship between BAP1
and PBRM1, we performed gene expression analyses. We grouped
tumors and tumorgrafts according to their BAP1 and PBRM1 sta-
tus and evaluated differences with respect to wild-type tumors and
tumorgrafts (**Fig. 5c**). Probe sets (probes) that we had previously
determined, using tumorgrafts, to be driven by non-neoplastic cells[21]
were excluded from the analysis. We identified 1,451 probes that were
deregulated in BAP1-deficient tumors relative to tumors that were
wild type for both *BAP1* and *PBRM1* ($q < 0.05$) (**Supplementary
Data 4**). A similar number of probes distinguished PBRM1-deficient
tumors (**Supplementary Data 4**). These two data sets had 94 probes in
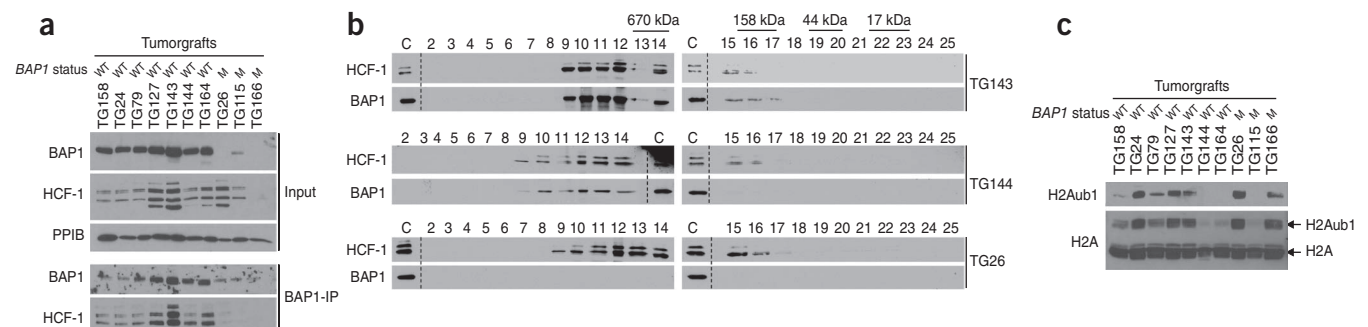common (**Fig. 5d**). However, the overlap expected to occur at random

Figure 4 BAP1 binds to and elutes with HCF-1 in tumorgrafts. (**a**) Protein blots of input and BAP1 immunoprecipitates (BAP1-IP) from the indicated
tumorgrafts. WT, wild type; M, mutant. (**b**) Protein blots of trichloroacetic acid (TCA)-precipitated gel-filtration fractions of tumorgrafts with either
wild-type (TG143 and TG144) or mutant (TG26) *BAP1*. C, control lysate from 769-P cells. (**c**) Protein blots of partially purified histone fractions from
tumorgrafts with the indicated *BAP1* status.

Figure 5 Loss of BAP1 and PBRM1 form the basis of a molecular genetic classification system for ccRCCs. (**a**) Representative hematoxylin and eosin (H&E) and IHC images of tumors with loss of BAP1, PBRM1 or both. Scale bar, 50 μm, 10 μm for inset. Open arrows, tumor cells; simple arrows, stroma and/or inflammatory cells; filled arrow, rhabdoid tumor cell. (**b**) Pie chart of the distribution of ccRCC subtypes. (**c**) Heatmap of statistically significant probes distinguishing *BAP1*- and *PBRM1*-deficient tumors and tumorgrafts relative to wild-type tumors and tumorgrafts. Expression of the same probes in renal cortex is included as a reference. The full data set is provided in **Supplementary Data 4**. (**d**) Venn diagram showing the overlap in *BAP1* and *PBRM1* gene expression signatures, with associated global pathway analyses.
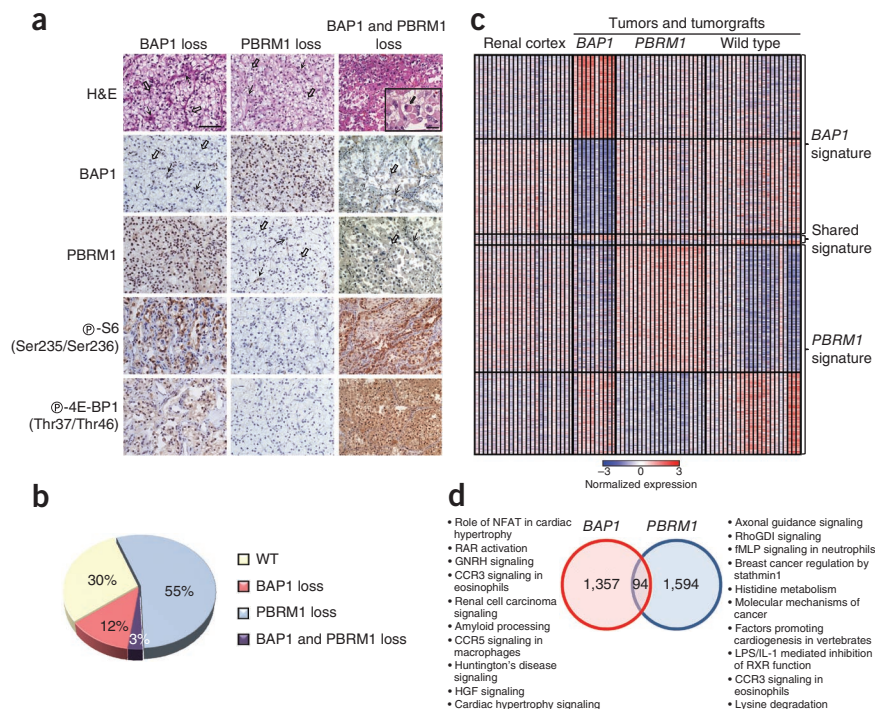
was 67. Similarly, pathway analyses of the two expression signatures showed little overlap. These results suggest that BAP1 and PBRM1 do not function in the same pathway and that the tumorigenic advantage to mutating *BAP1* and *PBRM1* is context dependent.

Further supporting the notion that loss of BAP1 and PBRM1 in tumors is not equivalent, analyses of the 176 tumors showed that PBRM1 loss was not associated with high tumor grade ($q = 0.26$) (**Supplementary Data 1**). In the 348 ccRCC tumors sequenced by the Sanger Institute[9,10] (**Supplementary Data 3**), we found a non-significant correlation between PBRM1 loss and low tumor grade ($P = 0.074$). Furthermore, when focusing the analyses of the 176 tumors on those that had exclusively lost PBRM1, a statistically significant correlation with low tumor grade was found ($q = 0.025$).

Tumors with loss of BAP1 and PBRM1 have rhabdoid features
A few tumors had loss of both *BAP1* and *PBRM1* ($n = 5$) (**Supplementary Data 1**). Although co-occurrence of mutations in tumors may not indicate their simultaneous presence in the same cell and there is substantial mutation heterogeneity in RCC[17,47], in two tumors for which tumorgrafts were available, MAR$_{TG}$ values for both *BAP1* and *PBRM1* were ~1, and no wild-type alleles were detected (data not shown). These data suggest that the two mutations were indeed present in the same tumor cells and highlight another application of tumorgrafts.

Tumors deficient in both BAP1 and PBRM1 were uniformly of high grade and showed characteristic features: abundant acidophilic cytoplasm, eccentric nuclei and prominent macronucleoli (**Fig. 5a**). These features were consistent with rhabdoid morphology[48], a form of dedifferentiation portending aggressive tumor behavior[49]. They were present in all tumors for which there was sufficient material for analysis (4/5), and, although not unique to tumors deficient in both BAP1 and PBRM1, the association was significant ($q = 0.0007$; **Supplementary Data 1**).

DISCUSSION
These results implicate *BAP1* as a tumor suppressor in ccRCC and establish the foundation for a molecular genetic classification of RCC. We show that 70% of ccRCCs lose either BAP1 or PBRM1, that tumors tend to segregate into BAP1- or PBRM1-deficient subtypes and that BAP1 loss but not PBRM1 loss is associated with high tumor grade.

BAP1 functions as a two-hit tumor suppressor in ccRCC, and, consistent with this, mutant *BAP1* does not act in a dominant-negative fashion. Both copies of *BAP1* are also lost in melanoma[28,29,50] and mesothelioma[30,51]. Although the number of RCC samples with *BAP1* mutations is small, it is notable that no second-hit point mutations or indels were observed. In contrast, both *BAP1* alleles may be inactivated through a point mutation (or indel) in mesothelioma[51]. We speculate that the different modes of inactivation of the second *BAP1* allele reflect tissue-specific tumor suppressor gene cooperativity. Indeed, in ccRCC, 3p loss may simultaneously inactivate several genes suppressing renal tumorigenesis, including, most importantly, *VHL*, which is rarely mutated in other tumor types. In metastatic uveal melanoma, whole chromosome 3 losses are frequent, and other melanoma metastasis suppressors may exist on 3q. Thus, the deletion architecture of tumors may reflect tissue-specific cooperativity of tumor suppressor genes.

We propose that subsequent to a *VHL* mutation, which likely represents an early event in tumorigenesis[17], the loss of 3p leaves cells vulnerable to the loss of the remaining *PBRM1* or *BAP1* allele. The acquisition of a *PBRM1* or *BAP1* mutation may set the course for ccRCCs with different properties. PBRM1 and BAP1 likely affect different epigenetic programs, and BAP1 loss is associated with high tumor grade and mTORC1 activation. Notably, whereas mutations in *SETD2*, which is also at 3p, seem to distribute equally between *PBRM1*-deficient and wild-type tumors, this is not the case for *BAP1* mutations. *PBRM1* and *BAP1* mutations anticorrelate in ccRCC. These data suggest that there is a genetic context to tumor suppressor function and that simultaneous loss of BAP1 and PBRM1 in most tumors is disadvantageous.

The clinical implications of BAP1 loss remain to be explored. As BAP1 loss was associated with high tumor grade and correlated with metastasis development in uveal melanoma[28], BAP1 loss in ccRCC may be associated with poor prognosis. From a therapeutic standpoint, whereas RCC is considered radioresistant, BAP1-deficient tumors may be more sensitive. Evaluating the prognostic and therapeutic implications of BAP1 loss will be greatly facilitated

by the development in a clinical laboratory of a highly sensitive and specific IHC assay.

Notably, *BAP1* is mutated in the germline, where it predisposes to melanoma and mesothelioma[28,29,50,51]. Given the role of BAP1 in sporadic ccRCC, germline *BAP1* mutations may similarly predispose to RCC. In fact, a germline variant (c.121G>A; p.Gly41Ser) was identified in one individual who had two first-degree relatives and one second-degree relative with RCC; this individual had previously been screened for a germline *VHL* mutation, but no mutation was found. In addition, a recently reported pedigree had one individual with a germline *BAP1* mutation who had RCC[51]. Thus, *BAP1* mutation in the germline may predispose to RCC, in which case, RCC development may also be initiated by loss of BAP1.

Multiple lines of evidence implicate HCF-1 in BAP1-mediated RCC tumor suppressor function. First, BAP1 binds to and cofractionates with HCF-1. Second, as determined in immunodepletion experiments, the majority of BAP1 is bound to HCF-1. HCF-1 is a very abundant protein[52], and this may explain why mutant BAP1 does not function as a dominant negative. Third, the growth inhibitory effect of BAP1 is compromised by a mutation that, although not disruptive to protein structure (as determined by retention of deubiquitinating activity), disrupts HCF-1 binding. Finally, the interaction with HCF-1 is unlikely to reflect an abnormal epigenetic state of tumor cell lines in culture, as BAP1 also binds to and cofractionates with HCF-1 in tumorgrafts. Notably, however, the HCF-1 binding motif in *BAP1* is not conserved in the *Drosophila* Calypso protein.

The role of H2Aub1 in ccRCC requires further study. BAP1 binding to HCF-1 was required for the suppression of cell proliferation but was dispensable for H2Aub1 deubiquitination. Thus, these two functions of BAP1—HCF-1 binding and H2Aub1 deubiquitination—can be separated. We did not find a correlation between BAP1 inactivation and global H2Aub1 levels in tumors. Nevertheless, the levels of H2Aub1 were not uniform across tumors, and we cannot rule out the possibility that BAP1 may affect the levels of H2Aub1 at specific sites.

Our studies were greatly aided by the availability of tumorgrafts. Tumorgrafts were instrumental in determining MARs with accuracy and for the identification of putative two-hit tumor suppressor genes. They also made it possible to determine the co-occurrence of mutations in tumor cells, and, when mutations occurred in regions of amplification, they shed light on the temporal sequence of mutation acquisition. Finally, tumorgrafts provided a renewable source of tumor material, allowing us to evaluate the relevance of biochemical observations made in cell lines in culture.

While this manuscript was in preparation, a brief communication reported a list of 12 genes mutated in ccRCC[53], including *TSC1*, which we previously showed to be mutated in sporadic ccRCC[18], and *BAP1*. The mutation frequency reported for *BAP1* was 8%, but a *VHL* mutation frequency of 27% suggests low sensitivity.

URLs. Bioconductor, http://www.bioconductor.org/; Catalogue of Somatic Mutations in Cancer (COSMIC), http://www.sanger.ac.uk/genetics/CGP/cosmic/; ImageJ, http://rsbweb.nih.gov/ij/; Integrative Genomics Viewer (IGV), http://www.broadinstitute.org/igv/.

METHODS
Methods and any associated references are available in the online version of the paper.

Accession codes. SNP and gene expression microarray data have been deposited at the Gene Expression Omnibus (GEO) (GSE25540 and GSE36895, respectively). Whole-genome and exome sequences for individuals consenting to the deposit of their information are in the database of Genotypes and Phenotypes (dbGaP) (phs000491).

Note: Supplementary information is available in the online version of the paper.

AUTHOR CONTRIBUTIONS
S.P.-L. processed, managed and extracted nucleic acids from tissues, evaluated and validated mutations, and performed bioinformatic analyses on the exome data, as well as copy-number, gene expression and statistical analyses. S.V.-R.-d.-C. was responsible for most biochemical studies using cell lines and tumorgrafts. A.L., T.H., S.J. and M.L. supervised the whole-genome sequencing process, performed quality control measures and were responsible for the primary SNV analysis in the clinical laboratory. N.L. analyzed exome sequences under the supervision of C.D.H. A.P.-J. and P.S. helped with tissue processing and histology. S.W. helped with functional studies in UMRC6 cells. T.Y. assisted in mutation validation and mouse studies. L.Z. reviewed patient's records. L.K. and N.G. performed *in silico* structural analyses for BAP1 and PBRM1. S.S. maintained the tumorgrafts and processed tissues. Y.L., V.M. and A.I.S. provided tissues and cell lines and assisted with the procurement of samples from the index subject. P.B.S. was the index subject's genetic counselor. W.K. and P.K. evaluated the pathology slides, and P.K. was responsible for the IHC assays. X.-J.X. performed statistical analyses and revised statistics. S.W.W.W. performed the indel analysis. M.T.R. and D.R.B. supervised and managed the genome sequencing and annotation process. J.B. conceived the study, designed experiments, analyzed the data and wrote the manuscript, with input from S.P.-L. and other authors.

1. Siegel, R., Ward, E., Brawley, O. & Jemal, A. Cancer statistics, 2011: the impact of eliminating socioeconomic and racial disparities on premature cancer deaths. *CA Cancer J. Clin.* **61**, 212–236 (2011).
2. Baldewijns, M.M. *et al.* Genetics and epigenetics of renal cell cancer. *Biochim. Biophys. Acta* **1785**, 133–155 (2008).
3. Brugarolas, J. Renal-cell carcinoma—molecular pathways and therapies. *N. Engl. J. Med.* **356**, 185–187 (2007).
4. Latif, F. *et al.* Identification of the von Hippel-Lindau disease tumor suppressor gene. *Science* **260**, 1317–1320 (1993).
5. Gnarra, J.R. *et al.* Mutations of the *VHL* tumour suppressor gene in renal carcinoma. *Nat. Genet.* **7**, 85–90 (1994).
6. Nickerson, M.L. *et al.* Improved identification of von Hippel-Lindau gene alterations in clear cell renal tumors. *Clin. Cancer Res.* **14**, 4726–4734 (2008).
7. Beroukhim, R. *et al.* Patterns of gene expression and copy-number alterations in von-hippel lindau disease-associated and sporadic clear cell carcinoma of the kidney. *Cancer Res.* **69**, 4674–4681 (2009).
8. Chen, M. *et al.* Genome-wide profiling of chromosomal alterations in renal cell carcinoma using high-density single nucleotide polymorphism arrays. *Int. J. Cancer* **125**, 2342–2348 (2009).
9. Varela, I. *et al.* Exome sequencing identifies frequent mutation of the SWI/SNF complex gene *PBRM1* in renal carcinoma. *Nature* **469**, 539–542 (2011).
10. Dalgliesh, G.L. *et al.* Systematic sequencing of renal carcinoma reveals inactivation of histone modifying genes. *Nature* **463**, 360–363 (2010).
11. van Haaften, G. *et al.* Somatic mutations of the histone H3K27 demethylase gene *UTX* in human cancer. *Nat. Genet.* **41**, 521–523 (2009).

12. Fuhrman, S.A., Lasky, L.C. & Limas, C. Prognostic significance of morphologic parameters in renal cell carcinoma. *Am. J. Surg. Pathol.* **6**, 655–663 (1982).
13. Bretheau, D. *et al.* Prognostic value of nuclear grade of renal cell carcinoma. *Cancer* **76**, 2543–2549 (1995).
14. Ficarra, V. *et al.* Prognostic and therapeutic impact of the histopathologic definition of parenchymal epithelial renal tumors. *Eur. Urol.* **58**, 655–668 (2010).
15. Pantuck, A.J. *et al.* Prognostic relevance of the mTOR pathway in renal cell carcinoma: implications for molecular patient selection for targeted therapy. *Cancer* **109**, 2257–2267 (2007).
16. Sabatini, D.M. mTOR and cancer: insights into a complex relationship. *Nat. Rev. Cancer* **6**, 729–734 (2006).
17. Gerlinger, M. *et al.* Intratumor heterogeneity and branched evolution revealed by multiregion sequencing. *N. Engl. J. Med.* **366**, 883–892 (2012).
18. Kucejova, B. *et al.* Interplay between pVHL and mTORC1 pathways in clear-cell renal cell carcinoma. *Mol. Cancer Res.* **9**, 1255–1265 (2011).
19. Brugarolas, J. Research translation and personalized medicine. in *Renal Cell Carcinoma* (eds. Figlin, R.A., Rathmell, W.K. & Rini, B.I.) 161–191 (Springer New York, 2012).
20. Hahn, S.A. *et al.* Allelotype of pancreatic adenocarcinoma using xenograft enrichment. *Cancer Res.* **55**, 4670–4675 (1995).
21. Sivanand, S. *et al.* A validated tumorgraft model reveals activity of dovitinib against renal cell carcinoma. *Sci. Transl. Med.* **4**, 137ra75 (2012).
22. Lee, S.T. *et al.* Mutations of the *P* gene in oculocutaneous albinism, ocular albinism, and Prader-Willi syndrome plus albinism. *N. Engl. J. Med.* **330**, 529–534 (1994).
23. Suzuki, T. *et al.* Six novel *P* gene mutations and oculocutaneous albinism type 2 frequency in Japanese albino patients. *J. Invest. Dermatol.* **120**, 781–783 (2003).
24. Gasparre, G., Romeo, G., Rugolo, M. & Porcelli, A.M. Learning from oncocytic tumors: why choose inefficient mitochondria? *Biochim. Biophys. Acta* **1807**, 633–642 (2011).
25. Jensen, D.E. *et al.* BAP1: a novel ubiquitin hydrolase which binds to the BRCA1 RING finger and enhances BRCA1-mediated cell growth suppression. *Oncogene* **16**, 1097–1112 (1998).
26. Ventii, K.H. *et al.* BRCA1-associated protein–1 is a tumor suppressor that requires deubiquitinating activity and nuclear localization. *Cancer Res.* **68**, 6953–6962 (2008).
27. Eletr, Z.M. & Wilkinson, K.D. An emerging model for BAP1's role in regulating cell cycle progression. *Cell Biochem. Biophys.* **60**, 3–11 (2011).
28. Harbour, J.W. *et al.* Frequent mutation of *BAP1* in metastasizing uveal melanomas. *Science* **330**, 1410–1413 (2010).
29. Wiesner, T. *et al.* Germline mutations in *BAP1* predispose to melanocytic tumors. *Nat. Genet.* **43**, 1018–1021 (2011).
30. Bott, M. *et al.* The nuclear deubiquitinase BAP1 is commonly inactivated by somatic mutations and 3p21.1 losses in malignant pleural mesothelioma. *Nat. Genet.* **43**, 668–672 (2011).
31. Misaghi, S. *et al.* Association of C-terminal ubiquitin hydrolase BRCA1-associated protein 1 with cell cycle regulator host cell factor 1. *Mol. Cell. Biol.* **29**, 2181–2192 (2009).
32. Nishikawa, H. *et al.* BRCA1-associated protein 1 interferes with BRCA1/BARD1 RING heterodimer activity. *Cancer Res.* **69**, 111–119 (2009).
33. Machida, Y.J., Machida, Y., Vashisht, A.A., Wohlschlegel, J.A. & Dutta, A. The deubiquitinating enzyme BAP1 regulates cell growth via interaction with HCF-1. *J. Biol. Chem.* **284**, 34179–34188 (2009).
34. Scheuermann, J.C. *et al.* Histone H2A deubiquitinase activity of the Polycomb repressive complex PR-DUB. *Nature* **465**, 243–247 (2010).
35. Yu, H. *et al.* The ubiquitin carboxyl hydrolase BAP1 forms a ternary complex with YY1 and HCF-1 and is a critical regulator of gene expression. *Mol. Cell. Biol.* **30**, 5071–5085 (2010).
36. Kristie, T.M., Liang, Y. & Vogel, J.L. Control of α-herpesvirus IE gene expression by HCF-1 coupled chromatin modification activities. *Biochim. Biophys. Acta* **1799**, 257–265 (2010).
37. Knez, J., Piluso, D., Bilan, P. & Capone, J.P. Host cell factor–1 and E2F4 interact via multiple determinants in each protein. *Mol. Cell. Biochem.* **288**, 79–90 (2006).
38. Tyagi, S., Chabes, A.L., Wysocka, J. & Herr, W. E2F activation of S phase promoters via association with HCF-1 and the MLL family of histone H3K4 methyltransferases. *Mol. Cell* **27**, 107–119 (2007).
39. Wysocka, J., Myers, M.P., Laherty, C.D., Eisenman, R.N. & Herr, W. Human Sin3 deacetylase and trithorax-related Set1/Ash2 histone H3–K4 methyltransferase are tethered together selectively by the cell-proliferation factor HCF-1. *Genes Dev.* **17**, 896–911 (2003).
40. Yokoyama, A. *et al.* Leukemia proto-oncoprotein MLL forms a SET1-like histone methyltransferase complex with menin to regulate Hox gene expression. *Mol. Cell. Biol.* **24**, 5639–5649 (2004).
41. Narayanan, A., Ruyechan, W.T. & Kristie, T.M. The coactivator host cell factor–1 mediates Set1 and MLL1 H3K4 trimethylation at herpesvirus immediate early promoters for initiation of infection. *Proc. Natl. Acad. Sci. USA* **104**, 10835–10840 (2007).
42. Liang, Y., Vogel, J.L., Narayanan, A., Peng, H. & Kristie, T.M. Inhibition of the histone demethylase LSD1 blocks α-herpesvirus lytic replication and reactivation from latency. *Nat. Med.* **15**, 1312–1317 (2009).
43. Smith, E.R. *et al.* A human protein complex homologous to the *Drosophila* MSL complex is responsible for the majority of histone H4 acetylation at lysine 16. *Mol. Cell. Biol.* **25**, 9175–9188 (2005).
44. Stokes, M.P. *et al.* Profiling of UV-induced ATM/ATR signaling pathways. *Proc. Natl. Acad. Sci. USA* **104**, 19855–19860 (2007).
45. Matsuoka, S. *et al.* ATM and ATR substrate analysis reveals extensive protein networks responsive to DNA damage. *Science* **316**, 1160–1166 (2007).
46. Kaelin, W. Jr. Molecular biology of clear cell renal carcinoma. in *Renal Cell Carcinoma* (eds. Figlin, R.A., Rathmell, W.K. & Rini, B.I.) 27–47 (Springer New York, 2012).
47. Xu, X. *et al.* Single-cell exome sequencing reveals single-nucleotide mutation characteristics of a kidney tumor. *Cell* **148**, 886–895 (2012).
48. Chapman-Fredricks, J.R. *et al.* Adult renal cell carcinoma with rhabdoid morphology represents a neoplastic dedifferentiation analogous to sarcomatoid carcinoma. *Ann. Diagn. Pathol.* **15**, 333–337 (2011).
49. Gökden, N. *et al.* Renal cell carcinoma with rhabdoid features. *Am. J. Surg. Pathol.* **24**, 1329–1338 (2000).
50. Abdel-Rahman, M.H. *et al.* Germline *BAP1* mutation predisposes to uveal melanoma, lung adenocarcinoma, meningioma, and other cancers. *J. Med. Genet.* **48**, 856–859 (2011).
51. Testa, J.R. *et al.* Germline *BAP1* mutations predispose to malignant mesothelioma. *Nat. Genet.* **43**, 1022–1025 (2011).
52. Wysocka, J., Reilly, P.T. & Herr, W. Loss of HCF-1-chromatin association precedes temperature-induced growth arrest of tsBN67 cells. *Mol. Cell. Biol.* **21**, 3820–3829 (2001).
53. Guo, G. *et al.* Frequent mutations of genes encoding ubiquitin-mediated proteolysis pathway components in clear cell renal cell carcinoma. *Nat. Genet.* **44**, 17–19 (2012).

ONLINE METHODS

Regulatory considerations. All subjects provided written informed consent to a UT Southwestern Institutional Review Board (IRB)–approved protocol for tissue collection for genetic studies. Whole-genome and exome sequences were released in the database of Genotypes and Phenotypes (dbGaP) for those individuals that gave explicit authorization on the consent form.

Annotation. Tumor samples were labeled with a number or a number preceded by a T if those samples were also used for tumorgraft generation. Tumorgrafts were labeled with the same number as tumors with the prefix TG and followed by a cohort c number (when applicable) referring to the tumor passage (for example, c0 for a primary tumorgraft).

Tumor stage was determined on the basis of tumor, node, metastasis (TNM) classification from the American Joint Committee on Cancer. Samples were annotated according to the edition corresponding to the date of surgery. Per the seventh edition, all tumors with lymph node metastases were referred to as pN1.

Tissue selection. ccRCC and adjacent normal kidney samples were frozen fresh in liquid nitrogen and stored at −80 °C. Tumor content and quality was inferred by a pathologist from perpendicular sections immediately flanking 1–3 mm thick fragments that were oriented using pathology dyes (**Supplementary Fig. 2c**). For whole-genome sequencing a sample was selected with ~90% tumor content in both sections. For the Discovery Set, 76 ccRCC samples with ≥80% tumor cellularity were selected among 431 fresh-frozen tumor samples from 133 patients. Seven tumor samples and a metastasis with ≥85% tumor cellularity were selected for exome sequencing among 16 patients with tumorgrafts growing in mice[43]. For the Validation Set, 92 ccRCC samples with ≥70% tumor cellularity were selected among 535 fresh-frozen tumor samples from 165 RCC patients. Genomic DNA and RNA were simultaneously extracted from each tissue (detailed in the **Supplementary Note**). Reference DNA, extracted from either adjacent normal kidney or peripheral blood mononuclear cells (PBMCs), was available for 71/76 tumors in the Discovery Set and 82/92 tumors of the Validation Set.

Whole-genome sequencing of paired-end libraries from tumor and matched normal genomes. Tumor and PBMC samples were processed in a CLIA-certified and College of American Pathologists (CAP)-accredited laboratory. The preparation of short-insert (212–263 bp) Illumina paired-end sequencing libraries, flow cells and clusters has been described previously[54]. Paired-end sequence reads of 100 bases were generated using the Genome Analyzer IIx. Image analysis, base calling and Phred quality scoring were performed using the Illumina analysis pipeline (RTA, v1.5). Sequence reads were filtered out from clusters whose proximity to others resulted in mixed sequence data.

Whole-genome somatic substitution and indel detection. Single-nucleotide variants (SNVs) from the reference sequence (human NCBI36.1) were determined separately for the tumor and normal genomes using CASAVA, v1.6. Prediction of a homozygous SNV required a minimum allele score of 10 (equivalent to at least three high-quality (Q33) base calls). Additionally, for heterozygous calls, the second allele was required to have a score of at least 6 (equivalent to two Q30 base calls), and the ratio of the two allele scores had to be ≤3, so that allele ratios did not deviate from the expected 1:1 ratio for heterozygous calls. Indels relative to human NCBI36.1 were predicted using GROUPER. SNVs and indels in tumors were only considered as candidate somatic events if the read depth at the equivalent site in the normal genome build was at least 10. SNVs and indels observed in both genomes were subtracted from the tumor calls. Previously known SNPs (those in dbSNP130) were also removed. Indels in the tumor overlapping a contig of assembled shadow reads in the normal genome were removed. The impact of somatic changes on protein-coding and non-coding genes was annotated using Ensembl version 54.

Exome capture and sequencing. Exome capture was performed by Illumina FastTrack using Illumina Truseq exome-target enrichment. Details are provided in the **Supplementary Note**.

Exome mutation detection and validation. The sequences of tumor, metastasis and normal samples were compared to NCBI reference sequence, and SNVs and indels were determined independently using CASAVA, v1.8.0a4, without any filtering. Mutations predicted in tumors that were also present in the corresponding normal samples were eliminated (**Supplementary Table 5**). Synonymous mutations were removed, and the resulting mutations were inspected visually using the Integrative Genomics Viewer (IGV; see URLs) to confirm their presence in tumor but not normal sequence reads (**Supplementary Table 5**). All genes with recurrent mutations were validated by Sanger sequencing (**Supplementary Table 7**). For the remaining genes, a mutation calling accuracy of >95% for 82 mutations would signify >90% accuracy for the whole cohort, according to a cumulative hypergeometric distribution. Sanger sequencing of 82 randomly selected mutations (proportional to the number of mutations in 7 tumors and 1 metastasis) showed 4 false positives (<5%), all of which had been scored on the basis of 2 mutant reads (**Supplementary Table 6**). Among the remaining genes, those with just two mutant reads (three) were inferred to represent false positives (**Supplementary Data 2**).

Mutation analyses and mutant allele ratios. SNVs and indels in chromatograms were scored with Mutation Surveyor, v3.30 and v3.98 (Softgenetics), using an overlapping factor of 0.2 and a dropping factor of 0.1. Reference sequences were obtained from NCBI. Only bidirectionally observed somatic mutations are reported. Mutations within 7 nt upstream or downstream of an exon boundary were considered to be splice-site mutations. A somatically acquired *PBRM1* variant outside this range (15 nt upstream of exon 8) was not included in the analyses (sample 78).

MARs refer to the fraction of mutant allele for a particular mutation over the sum of mutant and wild-type alleles (MAR of 1, only mutant allele detected; MAR of 0.5, mutant and wild-type alleles detected at similar frequencies). MARs were calculated by measuring the nucleotide intensities of chromatograms using ImageJ (see URLs) (whole-genome data) or with the Mutation Quantifier function of Mutation Surveyor, v3.98 (exome data). For indels, MARs were calculated by taking the average of the measurements of at least five nucleotides. MARs were scored as <0.10 if they accounted for <10% of all alleles but were clearly present in tumorgrafts. For Illumina tracings, MARs were calculated on the basis of the number of mutant over total reads.

Copy-number analyses. Genomic DNA was hybridized to Affymetrix SNP Arrays 6.0 at the Genome Science Resource (Vanderbilt University) using standard procedures. Several tumor and tumorgraft SNP arrays were previously evaluated for other purposes and have been reported elsewhere[21]. CEL files were quantile normalized with Partek Genomics Suite 6.5, adjusting for fragment length and probe sequence without background correction. Paired copy numbers for tumors and tumorgrafts were calculated from the intensities of the corresponding normal samples. Genotypes were estimated using the birdseed v2 algorithm in the Affymetrix Genotyping Console 4.0. Regions of allelic imbalance were identified by determining the allele-specific copy number for the primary tumor or tumorgraft with respect to normal DNA using the Partek Genomics Suite. Copy numbers were adjusted for local GC content and were segmented using Circulary Binary Segmentation (CBS)[55], where $\log_2$ ratios were analyzed with the DNAcopy package of Bioconductor in R (see URLs), considering a type I error ($\alpha = 0.001$) and a minimum segment size of 5 markers. Maximum and minimum allele-specific copy numbers were segmented independently by CBS.

Establishment and maintenance of tumorgrafts. Tumorgraft studies were approved by the UT Southwestern Institutional Animal Care and Use Committee (IACUC). Fresh tumor fragments (~2 mm in diameter) were implanted in the kidney of NOD/SCID mice as described elsewhere[21].

Gene expression analyses. RNA samples were labeled with biotin and hybridized to Affymetrix Human Genome U133 Plus 2.0 arrays by the UT Southwestern Microarray Core. Gene expression arrays on 13 of 29 tumors and tumorgrafts were previously evaluated to identify a tumor-specific signature and have been previously reported[21]. CEL intensity files were analyzed as described elsewhere[56]. Probe sets with nonspecific hybridization

were removed (8,696, 16%). Further, 2,443 probe sets representing signal attributed to a stromal and/or immune signature[21] were removed. Tumors and tumorgrafts with mutations in either *BAP1* or *PBRM1* (but not both) were compared to tumors and tumorgrafts that were wild type for both *BAP1* and *PBRM1* using *t* tests and a Benjamini-Hochberg false discovery rate (FDR) correction[57]. Probe sets with FDR *q* < 0.05 were analyzed with Ingenuity Pathways Analysis (IPA).

Statistics. To determine whether a correlation (inverse correlation) existed between regional DNA copy numbers and MAR_{TG} (or MAR_T), a two-tailed Spearman correlation test was used (data not normally distributed according to a Shapiro-Wilk test). Correlations were compared as previously described[58]. The *P* values for the identification of 2 or 3 additional gene mutations among the 76 individuals in the discovery set were calculated using a binomial distribution, assuming, on the basis of data from the index subject, that the probability of identifying a nonsynonymous mutation in a gene was 0.0022 (47 mutations among the 21,099 protein-coding genes annotated in the GRCh37.p6 assembly). All Fuhrman grade 3 and 4 samples were reviewed for the presence of rhabdoid features. For the Sanger Institute data set[9,10],

the highest tumor grade was used for each tumor. Throughout, a Fisher's exact test was used to determine whether there were nonrandom associations between two binary variables. A Benjamini-Hochberg FDR correction of *P* values (*q* values) was calculated to account for multiple comparisons[57]. SPSS Statistics 17.0 and SAS 9.0 were used to analyze data.

Primer sequences and antibody information are provided in **Supplementary Tables 9** and **10**, respectively. Further details and descriptions of other experimental methods and materials are available in the **Supplementary Note**.

54. Bentley, D.R. *et al.* Accurate whole human genome sequencing using reversible terminator chemistry. *Nature* **456**, 53–59 (2008).
55. Olshen, A.B., Venkatraman, E.S., Lucito, R. & Wigler, M. Circular binary segmentation for the analysis of array-based DNA copy number data. *Biostatistics* **5**, 557–572 (2004).
56. Peña-Llopis, S. *et al.* Regulation of TFEB and V-ATPases by mTORC1. *EMBO J.* **30**, 3242–3258 (2011).
57. Benjamini, Y. & Hochberg, Y. Controlling the false discovery rate—a practical and powerful approach to multiple testing. *J. R. Stat. Soc., B* **57**, 289–300 (1995).
58. Steiger, J.H. Tests for comparing elements of a correlation matrix. *Psychol. Bull.* **87**, 245–251 (1980).

Erratum: BAP1 loss defines a new class of renal cell carcinoma

Samuel Peña-Llopis, Silvia Vega-Rubín-de-Celis, Arnold Liao, Nan Leng, Andrea Pavía-Jiménez, Shanshan Wang, Toshinari Yamasaki, Leah Zhrebker, Sharanya Sivanand, Patrick Spence, Lisa Kinch, Tina Hambuch, Suneer Jain, Yair Lotan, Vitaly Margulis, Arthur I Sagalowsky, Pia Banerji Summerour, Wareef Kabbani, S W Wendy Wong, Nick Grishin, Marc Laurent, Xian-Jin Xie, Christian D Haudenschild, Mark T Ross, David R Bentley, Payal Kapur & James Brugarolas

In the version of this article initially published, the P value given in the abstract for the anticorrelation between *BAP1* and *PBRM1* mutations was given incorrectly as 9×10^{-6} instead of 3×10^{-5}. The definition of mutant allele ratios (MARs) in the text on p. 1 of the PDF has been corrected. The titles and legends of Figure 1 and Table 1 incorrectly stated that data were presented from multiple tumors and tumorgrafts; these have been corrected to reflect that data came from one index subject. The title of Figure 2 originally referred to mutated residues; this has now been corrected to state that alterations in BAP1 are shown. On p. 7 of the PDF the text has been corrected to state that "a few tumors had loss of both *BAP1* and *PBRM*," whereas the text originally incorrectly cited somatic mutations in both genes. The errors have been corrected in the HTML and PDF versions of the article.